

Selective reduction in epitaxial $\text{SrFe}_{0.5}\text{Co}_{0.5}\text{O}_{2.5}$ and its reversibility

Received: 14 November 2024

Accepted: 23 July 2025

Published online: 15 August 2025



Joonhyuk Lee¹, Yu-Seong Seo², Krishna Chaitanya Pitike³, Gwoon Kim⁴, Sangkyun Ryu¹, Hyeyun Chung¹, Su Ryang Park⁵, Sangmoon Yoon⁵, Younghak Kim⁶, Valentino R. Cooper⁷, Hiromichi Ohta⁸, Jinhyung Cho⁹ & Hyoungjeen Jeon¹✉

Oxygen-vacancy engineering in transition metal oxides enables programmable functionalities by modulating the valence states and local coordination of constituents. Here, we report the selective reduction of cobalt ions in epitaxial $\text{SrFe}_{0.5}\text{Co}_{0.5}\text{O}_{2.5}$ thin films under reducing gas environments, while iron ions remain unchanged. X-ray absorption spectroscopy reveals an absorption edge shift of 1.65 eV in the Co *L*-edge upon reduction, and multiplet simulations estimate a decrease in the average Co valence from $\text{Co}^{2.91+}$ to $\text{Co}^{2.00+}$. This site- and element-specific reduction leads to the formation of a structurally distinct oxygen-deficient phase stabilized by oxygen vacancies at tetrahedral sites, as confirmed by density functional theory. Optical spectroscopy reveals an increase in the bandgap from 2.47 eV to 3.04 eV, accompanied by enhanced transparency. Furthermore, simultaneous in situ diffraction and transport measurements confirm fully reversible redox-driven transitions among three phases: reduced defective perovskite, brownmillerite, and oxygen-rich perovskite phases. These findings demonstrate that selective redox control in multi-cation oxides enables the realization of chemically and functionally distinct oxygen-deficient phases.

Transition metal oxides (TMOs) exhibit diverse emergent properties that have enabled their application in energy storage, catalysis, superconductivity, and electronic devices^{1–6}. Among various tunable parameters, oxygen vacancies have emerged as a powerful handle to modulate the valence state, local structure, and associated functionalities of TMOs. In several systems, oxygen vacancy ordering leads to new structural phases, such as brownmillerite and infinite-layer configurations^{7–9}. These vacancy-engineered phases, governed by local site-preferential vacancy formation, are promising candidates for oxygen-driven programmable matter. The formation and dynamics of

oxygen vacancies under controlled environments—such as hydrogen, nitrogen, or argon—have been shown to critically influence the functional properties of perovskite oxides. Prior studies report reversible redox switching in SrCoO_y ⁸, oxygen deficiency-induced phase transitions in SrFeO_y ¹⁰, resistive switching behavior and vacancy ordering in brownmillerite films³, and modulation of vacancy behavior through multi-cation substitution^{1,11}.

Recent efforts have focused on stabilizing oxygen-deficient phases in TMOs, particularly in cobalt- and iron-based perovskites, due to their rich redox chemistry and structural flexibility^{9,12}. In cobalt oxides,

¹Department of Physics, Pusan National University, Busan, Korea. ²Department of Physics, Sungkyunkwan University, Suwon, Korea. ³Nuclear Sciences Division, Pacific Northwest National Laboratory, Richland, WA, USA. ⁴Graduate School of Information Science and Technology, Hokkaido University, Sapporo, Japan. ⁵Department of Physics and Semiconductor Science, Gachon University, Seongnam, Korea. ⁶Pohang Accelerator Laboratory, Pohang University of Science and Technology, Pohang, Korea. ⁷Materials Science and Technology Division, Oak Ridge National Laboratory, Oak Ridge, TN, USA. ⁸Research Institute for Electronic Science, Hokkaido University, Sapporo, Japan. ⁹Department of Physics Education, Pusan National University, Busan, Korea.

✉ e-mail: hjeon@pusan.ac.kr

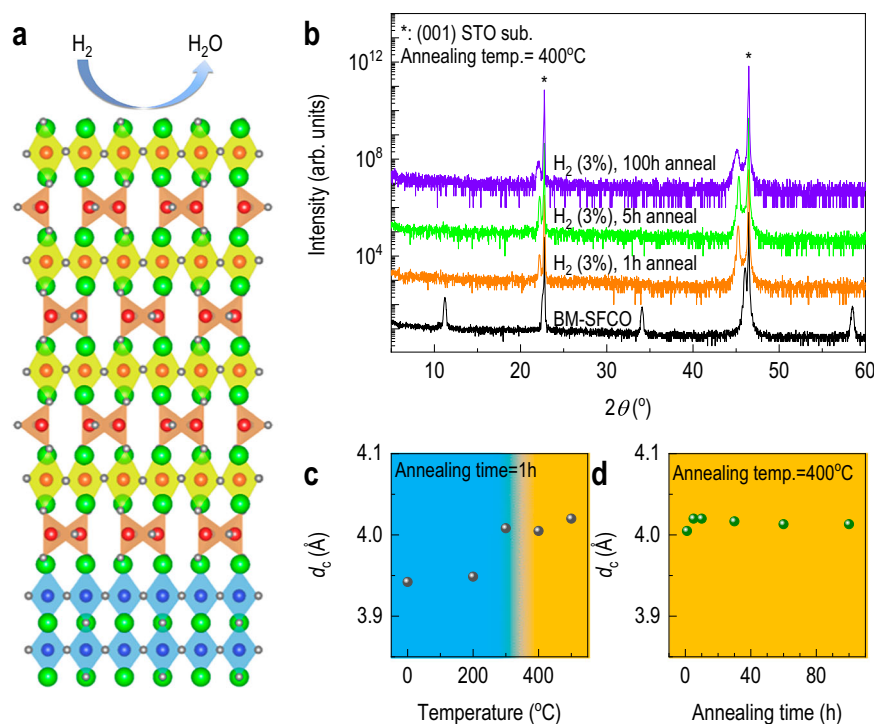


Fig. 1 | Structural evolution of $\text{SrFe}_{0.5}\text{Co}_{0.5}\text{O}_{2.5}$ (SFCO) during thermal reduction. **a** Schematic of the reduction process in brownmillerite SFCO thin films on (001) SrTiO_3 via annealing in 3% H_2/Ar forming gas. Green, red, blue, and grey spheres represent Sr, Fe/Co, Ti, and O atoms, respectively. **b** X-ray diffraction patterns of as-grown and reduced SFCO films. **c** Out-of-plane lattice constants as a

function of annealing temperature (1 h fixed). **d** Out-of-plane lattice constants as a function of annealing time at 400 °C. Blue and yellow background regions indicate the brownmillerite phase and the oxygen-deficient perovskite phase, respectively, emphasising the temperature range (300–400 °C) where the structural transition occurs.

phase transitions were typically limited between the perovskite and brownmillerite structures. However, a recent report on CaCoO_2 demonstrated the formation of an infinitely layered structure stabilized under strong reducing conditions, where the small ionic radius of Ca^{2+} may introduce chemical pressure and facilitates planar Co–O bonding¹³. In contrast, SrCoO_2 has been demonstrated to form a square spin-tube structure. This indicates that other factors, like chemical pressure from A-site cations, may hamper the formation of an infinitely layered structure in the Sr-based cobaltite^{4,14}. In contrast, iron oxides can adopt a wider range of oxygen stoichiometries without considering the chemical pressure. The associated transitions among perovskite (AFeO_3), brownmillerite ($\text{AFeO}_{2.5}$), and infinite-layer (AFeO_2) phases are often driven by apical oxygen removal and accompanied by notable structural contraction along the c-axis^{9,15}. However, the redox reactions in mixed B-site systems such as $\text{SrFe}_{1-x}\text{Co}_x\text{O}_{2.5}$ remain underexplored, particularly in terms of whether cooperative or competing interactions between Fe and Co can stabilize unique oxygen-deficient phases. In this study, we demonstrate that the reduction pathway of $\text{SrFe}_{0.5}\text{Co}_{0.5}\text{O}_{2.5}$ (SFCO) deviates from typical infinite-layer transitions. Instead, it leads to the formation of a defective perovskite phase stabilized by selective Co reduction and oxygen vacancy formation at tetrahedral sites, while Fe remains chemically inert. This behavior is distinct from both $\text{SrCoO}_{2.5}$, which decomposes under reducing conditions, and $\text{SrFeO}_{2.5}$, which retains its structure without substantial reduction. We attribute this structural stability to Fe incorporation, which modifies the local coordination environment and suppresses Co-induced structural collapse¹⁶. This behavior highlights the site- and element-specific nature of redox control in multication oxide systems and opens up a new phase space for programmable oxygen-deficient materials.

To systematically investigate the redox behavior of SFCO, we performed annealing experiments under reducing conditions using diluted hydrogen gas. A series of time- and temperature-dependent

studies revealed the formation of a distinct structure in SFCO, which is different from the brownmillerite or infinite-layer phases. To assess the compositional dependence, we extended our study to brownmillerite $\text{SrFe}_{1-x}\text{Co}_x\text{O}_{2.5}$ with $x = 0, 0.2$, and 1.0 . Notably, the Fe-rich sample ($x = 0$) retained its brownmillerite structure, showing only a crystallographic axis rotation consistent with previous studies¹⁷. In contrast, the Co-rich sample ($x = 1.0$) underwent structural decomposition, accompanied by the formation of CoO impurity. The intermediate composition ($x = 0.2$) exhibited no sign of structural change. These observations highlight the unique redox stability of the $x = 0.5$ composition, where the incorporation of Fe plays a crucial role in maintaining structural coherence and preventing decomposition^{11,13,18}. The cooperative yet asymmetric redox response of Fe and Co in the SFCO system stabilizes an oxygen-deficient defective perovskite phase that cannot be accessed in single-cation systems.

Results and discussion

Structural transformation via thermal reduction

To reduce the oxygen content in the as-grown brownmillerite (BM) SFCO thin films, we performed post-annealing in a 3% H_2/Ar forming gas (FG), which facilitates the removal of lattice oxygen via reaction with hydrogen (Fig. 1a). Films were annealed at various temperatures for 1 hour to investigate temperature-dependent structural evolution. X-ray diffraction (XRD) patterns (Fig. 1b and Supplementary Fig. 1) show that the BM structure is preserved up to 300 °C, with progressive out-of-plane lattice expansion indicating gradual oxygen vacancy formation¹⁹. Upon annealing at 400 °C and 500 °C, we observed an abrupt shift in the 008 diffraction peak to lower angles and the disappearance of the 006 diffraction peak, suggesting the collapse of BM ordering and the emergence of a new reduced phase (Fig. 1c). Annealing at 600 °C led to complete loss of diffraction peaks, indicating a breakdown of epitaxial order.

To further investigate the time-dependent stability of the reduced phase, we fixed the annealing temperature at 400 °C and varied the annealing time. As shown in Fig. 1d and Supplementary Fig. 2, out-of-plane lattice expansion continued up to 5 hours, reaching -4.020 Å, but remained unchanged thereafter up to 100 hours, indicating that the reduced phase is thermodynamically stabilized after extended reduction. Importantly, in-plane XRD measurements (Supplementary Fig. 3) confirm that the in-plane lattice parameters are locked by substrate-induced strain from SrTiO₃ substrate throughout the reduction process. This anisotropic lattice evolution strongly contrasts with the *c*-axis contraction, which is typically found in an infinite-layer structure, suggesting that the reduced phase is structurally distinct. Further structural analyses using reciprocal space mapping (RSM, Supplementary Fig. 4) and HAADF-STEM (Supplementary Fig. 5) reveal out-of-plane peak shifts and a Sr–Sr lattice expansion in the vertical direction, while the in-plane periodicity is preserved. The extracted lattice constants from these measurements are summarized in Supplementary Table 1 and show excellent agreement between the XRD and STEM results. Taken together, these observations indicate that the reduced SFCO does not transform into a planar infinite-layer phase, but instead evolves into an oxygen-deficient defective perovskite^{4,14,16}. The lack of long-range superstructure peaks suggests that oxygen vacancies are not ordered.

To understand the formation and stability of the reduced SFCO phase, we performed systematic annealing experiments on BM-SrFe_{1-x}Co_xO_{2.5} films with various compositions ($x = 0, 0.2, 0.5$, and 1.0), grown under identical conditions and annealed at 400 °C for 5 hours in FG. As summarized in Supplementary Fig. 6, the annealed BM-SrFeO_{2.5} ($x = 0$) retained its BM structure, with a minor crystallographic rotation similar to prior observations under vacuum annealing¹⁷. In contrast, BM-SrCoO_{2.5} ($x = 1.0$) decomposed into a CoO impurity phase, as evidenced by XRD^{20,21}. For BM-SrFe_{0.8}Co_{0.2}O_{2.5} with $x = 0.2$, no structural transformation was observed, indicating limited reduction. Notably, only the $x = 0.5$ composition led to a distinct structural change upon reduction, highlighting the critical role of Fe/Co ratio in determining redox behavior and phase stability.

While Fe remains chemically stable under these reducing conditions, its presence appears to suppress structural collapse by resisting apical oxygen removal, enabling the formation of a stable oxygen-deficient phase. This observation is consistent with prior reports showing that Fe-based perovskites can maintain structural coherence under reducing conditions⁹, whereas Co-based systems often decompose^{4,21,22}. Note that X-ray reflection revealed an increase in film thickness after reduction (23.40 nm for the as-grown SFCO and 24.30 nm for the reduced SFCO; Supplementary Fig. 7), consistent with the out-of-plane lattice expansion. When converted to unit cell layers, both films show comparable values (19.7 for the as-grown SFCO and 20.1 for the reduced SFCO), confirming that the reduction proceeds without significant structural degradation, while maintaining volumetric integrity. Atomic force microscopy images further revealed that the step-terrace morphology was preserved in both the as-grown and reduced films (Supplementary Fig. 8), indicating that the reduction process does not deteriorate surface integrity. The consistent root-mean-square roughness supports the conclusion that the reduced phase maintains high structural quality, without degradation of surface morphology. These results reinforce that the epitaxial strain is maintained in the reduced phase, while oxygen vacancies are accommodated within the lattice. To evaluate the thermal stability of the reduced phase, we conducted additional annealing at 500 °C. As shown in Supplementary Fig. 9, XRD and X-ray absorption spectroscopy (XAS) measurements after prolonged annealing revealed spectral broadening and structural degradation, indicating that the oxygen-deficient phase becomes unstable at the higher temperatures. This suggests an upper thermal limit for the reversible redox functionality in SFCO films.

Element-specific redox responses of Fe and Co

To determine whether the observed structural transformation arises from oxygen vacancy formation, we performed soft XAS at the Fe and Co *L*-edges. Figure 2a shows the Fe *L*-edge spectra for the as-grown and reduced SFCO films (annealed for 1, 5, and 100 hours). The spectral shape remains nearly unchanged, closely resembling that of LaFeO₃ and SrFe_{0.8}Co_{0.2}O_{2.5}, indicating that the Fe valence state is largely unaffected by the reduction process^{12,23}. In contrast, the Co *L*-edge spectra exhibit significant changes upon annealing, as shown in Fig. 2b²⁰. An absorption edge shift of 1.65 eV toward lower energies is observed for the Co *L*₃-edges, consistent with a reduction in oxidation state²⁴. To quantify the Co valence states, we performed multiplet simulations using the charge transfer multiplet for X-ray absorption spectroscopy (CTM4XAS)²⁵ code, a ligand-field multiplet framework that enables detailed modeling of transition metal *L*-edge spectra. The experimental spectrum was fitted by a linear combination of Co⁴⁺ and Co²⁺ configurations, revealing a decrease in the average Co valence from Co^{2.91+} of the as-grown to Co^{2.00+} of the reduced (Fig. 2c and Supplementary Figs. 10). These results indicate that the structural transformation is driven by selective Co reduction, while Fe remains chemically inert.

To support this estimation, we performed multiplet simulations using CTM4XAS to fit the Fe and Co *L*-edge spectra. To refine the CTM4XAS simulations, we included multiple coordination environments for each oxidation state. For Fe, four components were considered: Fe⁴⁺ (octahedral), Fe³⁺ (octahedral and tetrahedral), and Fe²⁺ (tetrahedral), based on prior reports identifying Fe³⁺ species in both sites under strain or oxygen-deficient conditions^{26,27}. Co spectra were simulated using Co⁴⁺ (octahedral) and Co²⁺ (tetrahedral), consistent with known valence distributions in cobaltite^{24,28}. The Fe *L*-edge spectrum showed a dominant Fe³⁺ character (Fe⁴⁺: Fe³⁺: Fe²⁺ = 2.80: 93.74: 3.46), corresponding to an estimated oxygen stoichiometry of SrFe_{0.5}Co_{0.5}O_{2.497}. The Co *L*-edge fitting yielded a Co⁴⁺: Co²⁺ ratio of 45.34: 54.66, corresponding to SrFe_{0.5}Co_{0.5}O_{2.453}. The combined analysis supports an overall oxygen content of SrFe_{0.5}Co_{0.5}O_{2.475 ± 0.022} for the as-grown film, consistent with the BM phase. The simulated spectral weights and corresponding oxygen stoichiometry estimates for both Fe and Co *L*-edges are summarized in Fig. 2c. These results stand in contrast to previous reports on mixed B-site perovskites, such as SrFe_{1-x}Cu_xO_{3-δ} and SrFe_{1-x}Co_xO_{3-δ}, where both B-site cations exhibited simultaneous redox behavior, yet no structurally distinct oxygen-deficient phase was stabilized under comparable reducing conditions^{29,30}.

We further investigated the element-specific magnetic response using X-ray magnetic circular dichroism (XMCD) at the Fe and Co *L*-edges at 130 K. As shown in Supplementary Fig. 11, only the O₂-annealed (O₂, 400 °C, 5 h anneal) sample exhibited discernible XMCD signals, confirming the presence of finite magnetic moments in the oxidized phase (SrFe_{0.5}Co_{0.5}O_{2.5+δ}). In contrast, no XMCD signal was detected in either the as-grown or reduced samples, suggesting the absence of net magnetic moments. These valence changes correlate with the anisotropic lattice evolution observed in RSM and STEM analyses, supporting the formation of an oxygen-deficient defective perovskite phase.

To further verify the element-specific valence changes associated with reduction, we examined the O *K*-edge XAS of SFCO films before and after annealing (Fig. 2d). In the reduced film, the feature within the 527.8–531.1 eV range, typically associated with Co 3*d*–O 2*p* hybridization³¹, is significantly suppressed, consistent with the removal of oxygen atoms near Co sites. In contrast, a pronounced intensity enhancement is observed near 533 eV. This spectral feature, measured in total electron yield (TEY) mode, has previously been attributed to the σ* resonance of surface-stabilized O₂⁻ superoxide species in oxygen-deficient cobalt oxides³². The formation of these species is facilitated by oxygen vacancies and the reduced transition metal

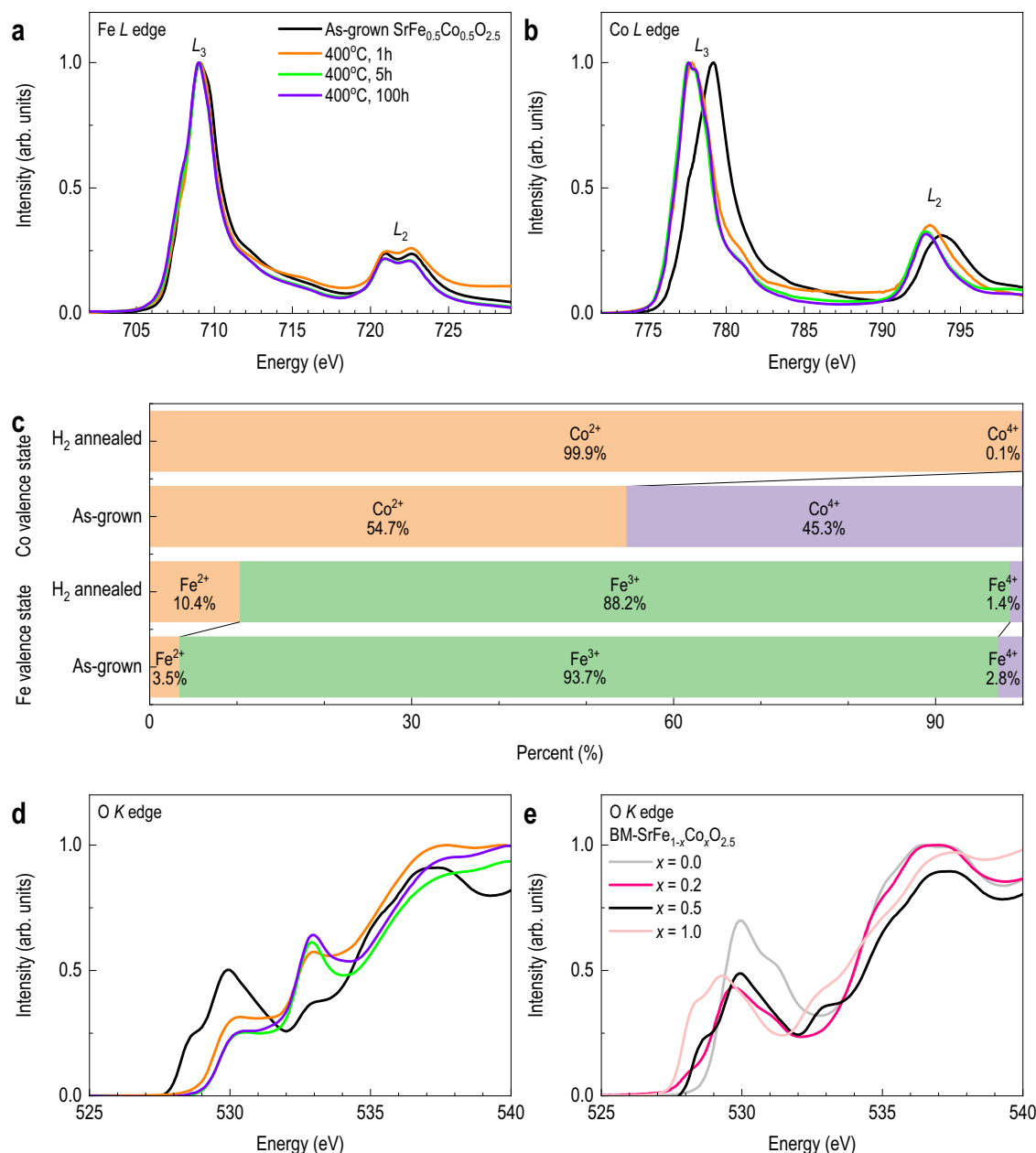


Fig. 2 | Element-specific electronic structure evolution upon reduction. X-ray absorption spectra (XAS) of (a) Fe L-edge and (b) Co L-edge for as-grown and reduced SrFe_{0.5}Co_{0.5}O_{2.5} (SFCO) films. c Estimated Fe and Co valence states from multiplet fitting. Lists relative proportions of Fe⁴⁺, Fe³⁺, Fe²⁺ and Co⁴⁺, Co²⁺ in as-

grown and 5 h reduced films. d O K-edge XAS spectra for SFCO films before and after reduction, showing changes in hybridization. e O K-edge XAS spectra for SrFe_{1-x}Co_xO_{2.5} with different x values.

states, particularly near the film surface³³. To further elucidate the element-specific hybridization, we measured the O K-edge spectra of BM-SrFe_{1-x}Co_xO_{2.5} with varying x values (x = 0.0, 0.2, 0.5, and 1.0) (Fig. 2e). The spectral region from 530 to 535 eV reflects hybridization between transition metal 3d and O 2p orbitals, with contributions from both Fe 3d–O 2p (near 529.5–530.5 eV) and Co 3d–O 2p (within 527.8–531.1 eV) interactions. These compositional spectra serve as fingerprints to distinguish local oxygen environments in mixed B-site perovskites. Quantitative multiplet fitting, summarized in Fig. 2c, confirms that the selective reduction of Co is accompanied by oxygen deficiency, further validating the proposed redox mechanism. Additionally, electron energy loss spectroscopy (EELS) measurements (Supplementary Fig. 12) show a discernible chemical shift in the Co L₃-edge toward lower energy after annealing, confirming the reduction of

cobalt ions. This local electronic structure change is consistent with the observed O K-edge spectral evolution and supports our interpretation of Co-selective reduction. In contrast, no significant energy shift was observed for the Fe L-edge in the EELS spectra, further supporting the conclusion that iron remains largely chemically inert during the reduction process.

Role of the apical oxygen sites and Co-selective reduction pathway

To gain atomistic insight into the site preference of oxygen vacancies and the mechanism underlying Co-selective reduction, we performed density functional theory (DFT) calculations (Fig. 3). We evaluated the oxygen vacancy formation enthalpy for three distinct oxygen sites in the BM-SFCO structure^{34–39}: equatorial oxygen within the octahedral

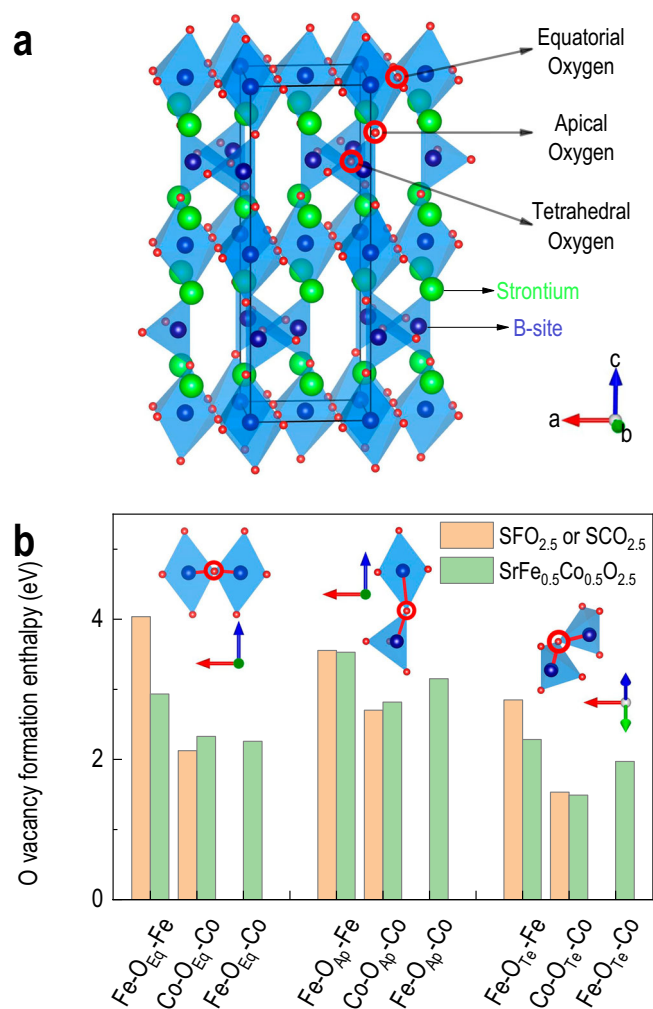


Fig. 3 | DFT calculations of oxygen vacancy formation. **a** Atomic structure of brownmillerite SFCO indicates three inequivalent oxygen sites. In the schematic, green, blue, and red spheres represent Sr, Fe/Co, and O atoms, respectively. **b** Computed oxygen vacancy formation enthalpies at different oxygen sites and B-site configurations.

layers, tetrahedral oxygen within the tetrahedral layers, and apical oxygen connecting tetrahedral and octahedral layers, as illustrated in Fig. 3a.

Since the experimental results indicate a selective reduction of Co ions while Fe remains largely unchanged, we considered different cationic environments surrounding each oxygen site, including Fe–Fe, Fe–Co, and Co–Co configurations. As shown in Fig. 3b, the formation enthalpy for oxygen vacancies is consistently lower when the oxygen is coordinated by Co-containing pairs. For instance, while Fe–O–Fe configurations at equatorial sites yield vacancy formation enthalpies close to 3 eV, Co–O–Co and Co–O–Fe configurations result in significantly lower values around 2 eV. This suggests that cobalt incorporation into the local environment promotes easier vacancy formation. Notably, even in Fe–O–Fe geometries, the enthalpy decreases as more Co atoms are introduced into the simulation cell, implying that the second-nearest neighbour also affects vacancy energetics.

When comparing different geometric sites for the same Co–Fe composition ($x = 0.5$), the tetrahedral oxygen sites exhibit the lowest average vacancy formation enthalpy (1.97 eV), followed by equatorial sites (2.25 eV), while apical sites show the highest average value

(>3 eV). These trends confirm that oxygen vacancies preferentially form at tetrahedral sites in SFCO. This pathway contrasts sharply with the infinite-layer phase formation, which requires removal of apical oxygen atoms to induce square-planar coordination and c -axis contraction. Our DFT calculations demonstrate that, in general, the removal of oxygen ions from apical sites is relatively difficult when compared to equatorial sites. Combined with the random distribution of Co and Fe ions, it is expected that there will be randomized oxygen coordination in the reduced SFCO. In addition, XRD and STEM do not show superlattice peaks or electron diffraction patterns associated with long-range vacancy ordering but indicate the expansion of the lattice along the out-of-plane direction. This suggests that the oxygen vacancies, while site-selective, are likely disordered at the macroscopic scale, resulting in a defective perovskite phase without long-range structural modulation.

Therefore, we interpret the reduced phase as an oxygen vacancy-stabilized defective perovskite with local site selectivity, rather than a vacancy-ordered phase. These findings have important implications for the reduction mechanism in SFCO. Unlike infinite-layer phases, where they are developed via removal of apical oxygen and lattice contraction, our data suggest that the reduction proceeds mainly via tetrahedral oxygen removal, leading to a structurally stable, anisotropic, and defective perovskite phase. This interpretation aligns with our experimental observations of c -axis expansion and preserved in-plane coherence during reduction (Supplementary Fig. 3). Furthermore, our results support a pathway distinct from both SrFeO_y and SrCoO_y , where $\text{SrFeO}_{2.5}$ typically maintains its BM structure under mild reducing conditions and $\text{SrCoO}_{2.5}$ decomposes into CoO-like phases^{9,15,40,41}. In contrast, our SFCO films exhibit a cooperative but asymmetric redox behavior, selective reduction of Co accompanied by retention of the Fe valence state, leading to the emergence of a stable oxygen-deficient phase (Supplementary Fig. 6). This site-specific redox pathway has not been observed in conventional single-cation perovskites and underscores the potential for achieving programmable oxygen-vacancy configurations in multi-cation systems^{9,15,40,42}. Selective Co reduction in SFCO, particularly at tetrahedral sites, enables a structural and electronic landscape that is chemically and functionally distinct from previously reported perovskite and infinite-layer oxides.

Suppression of inter-band transition and bandgap tuning via selective reduction

To further investigate the electronic consequences of selective cobalt reduction and oxygen vacancy formation, we examined the optical properties of $\text{SrFe}_{1-x}\text{Co}_x\text{O}_{2.5}$ films using spectroscopic ellipsometry. Figure 4a shows the optical conductivity spectra of BM- $\text{SrFe}_{1-x}\text{Co}_x\text{O}_{2.5}$ films with varying Fe/Co compositions. For BM- $\text{SrCoO}_{2.5}$ ($x = 1.0$), two distinct absorption peaks appear near 1.5 eV and 2.5 eV, corresponding to d – d and p – d transitions, respectively, consistent with prior reports^{43,44}. In contrast, BM- $\text{SrFeO}_{2.5}$ ($x = 0.0$) displays peaks near 2.7 eV and 4.0 eV, attributed to p – d transitions involving Fe–O hybridization^{10,45}. The $\text{SrFe}_{1-x}\text{Co}_x\text{O}_{2.5}$ films with $x = 0.2$ and 0.5 exhibit intermediate spectral features, reflecting a combination of Fe- and Co-related optical transitions. Notably, incorporation of Co leads to suppression of the 4 eV peak and enhanced spectral weight below 3 eV.

To track the evolution of optical properties upon reduction, we measured the optical conductivity spectra of the $x = 0.5$ films annealed for various durations. A significant decrease in optical conductivity between 2 eV and 3.7 eV was observed after reduction, while the high-energy peak near 4 eV remained largely unchanged (Fig. 4b). This behavior suggests that the suppressed spectral weight is primarily associated with Co–O transitions, consistent with the selective Co reduction observed by XAS. Additionally, the optical bandgap increased from 2.47 eV (as-grown SFCO) to 3.04 eV (reduced SFCO), indicative of enhanced transparency^{8,46}. This transition is visually confirmed in the inset of Fig. 4, where reduced films appear

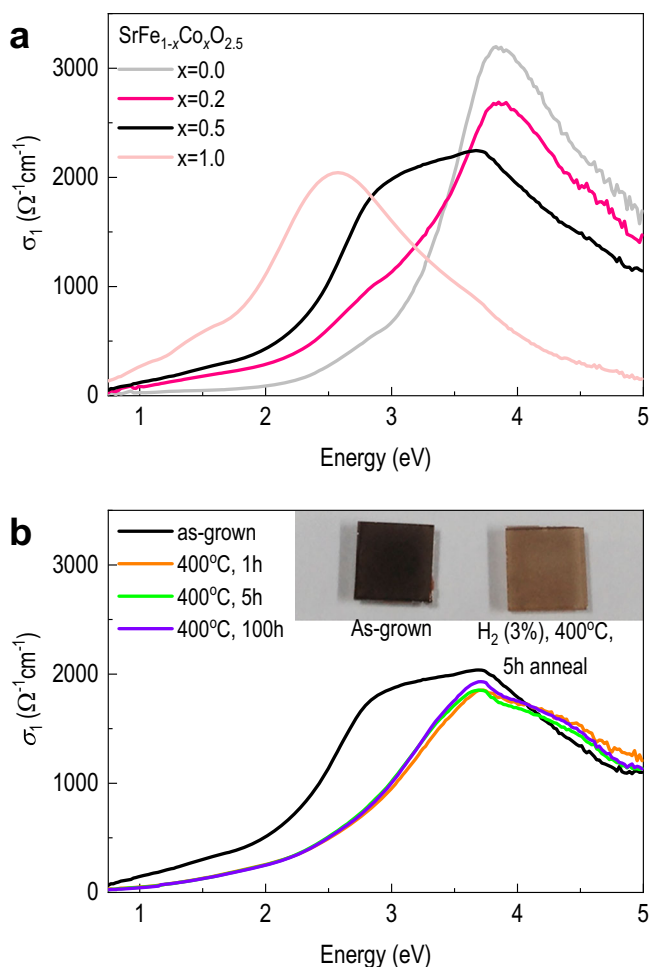


Fig. 4 | Optical properties of brownmillerite and reduced SFCO films. a Optical conductivity spectra of $\text{SrFe}_{1-x}\text{Co}_x\text{O}_{2.5}$ films ($x = 0, 0.2, 0.5$, and 1.0), showing composition-dependent absorption features. **b** Optical conductivity spectra of $\text{SrFe}_{0.5}\text{Co}_{0.5}\text{O}_{2.5}$ before and after reduction, highlighting spectral weight suppression and bandgap widening from 2.47 eV to 3.04 eV . Inset: photographs of as-grown (dark and opaque) and reduced (lighter and partially transparent) films on SrTiO_3 , visually confirming enhanced transparency upon reduction.

significantly lighter and more transparent than the as-grown samples. Such tunable optical responses, achieved via chemical reduction, highlight the potential of oxygen-deficient SFCO phases for optoelectronic/electrochromic applications requiring bandgap control and visible transparency.

Reversible redox transitions and formation of multiple distinct states in SFCO thin films

To explore the reversibility of phase transitions in SFCO, we performed simultaneous in situ experiments under controlled gas environments. These experiments revealed the presence of three structurally and electronically distinct states: the BM phase, the oxygen-deficient reduced phase, and the oxygen-rich perovskite-like phase. These states were identified through simultaneous monitoring of lattice parameters and resistance (Fig. 5) and further corroborated by the appearance or disappearance of BM superlattice reflections (Supplementary Fig. 13).

Initially, the SFCO film was annealed at 400°C under FG for ~ 2.5 hours, leading to the formation of the reduced phase. When the atmosphere was switched to high-purity N_2 at the same temperature, no noticeable change in either lattice constant or electrical resistance was observed, indicating that the reduced phase is structurally and

electronically stable under inert conditions. Subsequent annealing in pure O_2 gas at 400°C induced a rapid decrease in both lattice constant (Fig. 5a) and electrical resistance (Fig. 5b), suggesting re-oxidation toward an oxygen-rich SFCO phase. Notably, this transition occurred without abrupt changes in transport or diffraction signatures, indicating a continuous, diffusion-driven oxidation process. However, full oxidation to an ideal $\text{SrFe}_{0.5}\text{Co}_{0.5}\text{O}_3$ phase was not achieved under these conditions, likely due to limited oxygen partial pressure. Previous studies have shown that such full oxidation requires high-pressure oxygen or ozone treatments^{40,41,47}.

The resistance evolution mirrors the redox-induced structural changes: reduction led to charge localization and increased resistivity, while oxidation enhances carrier delocalization and reduces resistivity. This interplay reflects an intrinsic trade-off between optical transparency and electrical conductivity. While reduction enhances transparency and widens the bandgap, it simultaneously drives the material toward an insulating state. The ability to modulate both optical transparency and electrical conductivity via controlled redox tuning suggests that SFCO thin films could be promising candidates for multifunctional devices, including resistive switching memory and optoelectronic modulators^{48–54}.

Upon switching the atmosphere to high-purity N_2 at the same temperature, we observed a slight increase in the lattice constant and a corresponding increase in resistance. Expanded-range in situ XRD patterns revealed the reappearance of superlattice peaks such as 006_{BM} and 0010_{BM} , indicating partial reversion to the BM structure. This transformation is attributed to oxygen loss from the oxygen-rich perovskite-like state under inert conditions. To rule out the potential effect of residual oxygen during N_2 annealing, we performed control experiments under high-purity N_2 ⁵⁵. The absence of structural degradation or phase decomposition under N_2 annealing is confirmed by XRD in Supplementary Fig. 14. As shown in Supplementary Fig. 15, no structural degradation was observed even after multiple redox cycles (up to six cycles of alternating FG and O_2 annealing), confirming that the reduced phase is a structurally stable defective perovskite. The transient appearance of BM peaks upon switching from O_2 to N_2 (Supplementary Fig. 13) further supports an oxygen-mediated transformation pathway. After prolonged annealing in N_2 , we observed a saturation in both resistance and lattice contraction. These values, however, did not fully return to the initial BM levels observed in the reduced state¹². Switching back to FG restored the reduced phase lattice constant and electrical resistance, confirming the repeatability of the redox transition. Additional redox cycling experiments (Supplementary Fig. 15) further demonstrated stable and reversible switching between the three phases without structural degradation, underscoring the robustness of the oxygen-deficient phase under cyclic operation. Note that it is important to clarify that while we identify three structurally distinct states, BM, reduced defective perovskite, and oxygen-rich SFCO, these classifications are based primarily on their transport and diffraction signatures.

In this study, we demonstrated the selective reduction of Co ions in epitaxial SFCO thin films while maintaining the chemical inertness of Fe ions. Through a combination of soft X-ray absorption spectroscopy, density functional theory calculations, and spectroscopic ellipsometry, we revealed that oxygen vacancies preferentially form near Co sites, leading to the formation of an oxygen-deficient defective perovskite phase. This phase exhibits a widened optical bandgap and enhanced transparency compared to the BM phase, without significant structural degradation. Comparative experiments on $\text{SrFe}_{1-x}\text{Co}_x\text{O}_{2.5}$ with varying x compositions confirmed that the presence of Fe plays a crucial role in stabilizing the reduced phases. While Co-rich samples ($x = 1.0$) decomposed into impurity phases, Fe-rich and intermediate compositions ($x = 0.0, 0.2$, and 0.5) preserved structural coherence upon reduction, with $x = 0.5$ showing distinct defective perovskite formation. The incorporation of Fe modifies the local coordination

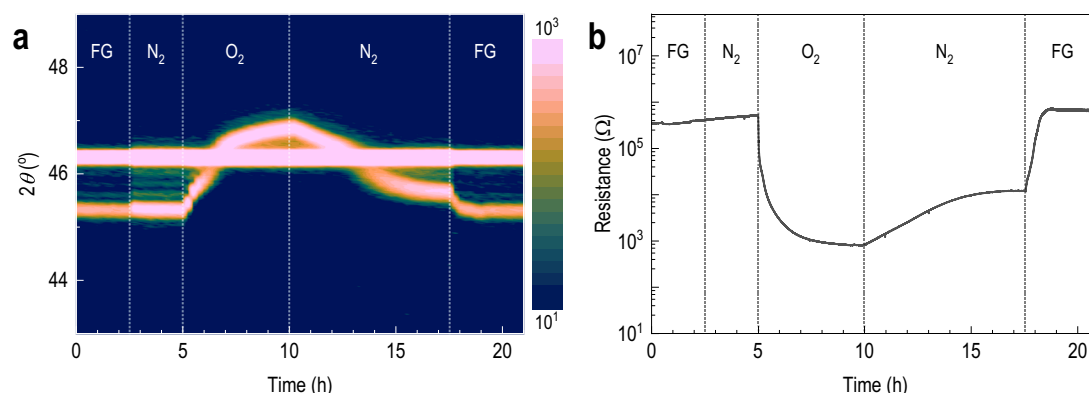


Fig. 5 | In situ monitoring of phase reversibility. **a** In situ x-ray diffraction and **b** resistance measurements during sequential 3% H₂/Ar forming gas switching at 400 °C, showing structural reversibility and electronic modulation among three distinct phases.

environment, suppressing Co-induced collapse and promoting the stability of oxygen-deficient phases under reducing conditions. Our findings highlight the cooperative yet asymmetric redox behavior in multi-cation oxide systems, offering a new avenue for programmable oxygen-vacancy engineering and multifunctional oxide design. The selective control of cation-specific reduction not only enables tunable optical and electronic properties but also offers insights into the design of robust, multifunctional perovskite oxides for future device applications.

Methods

Material synthesis

Epitaxial thin films of SrFe_{1-x}Co_xO_{2.5}, with compositions $x = 0.0, 0.2, 0.5$, and 1.0 , were grown on single-crystalline SrTiO₃ (001) substrates by pulsed laser deposition (PLD). The deposition was carried out at 600 °C under an oxygen partial pressure of 100 mTorr. A pulsed Nd:YAG laser (energy density: 0.75 J cm⁻², repetition rate: 4 Hz) was used as the ablation source. All substrates were pre-treated via standard thermal annealing to ensure atomically flat step-and-terrace morphology (Supplementary Fig. 8)⁵⁶. After deposition, the films were cooled to room temperature under the same oxygen partial pressure. Film thicknesses were measured using X-ray reflectivity, and structural characterization was conducted with a high-resolution X-ray diffractometer (D8 Discover, Bruker). Reciprocal space mapping confirmed that all films remained fully strained to the SrTiO₃ substrate. Post-deposition annealing was performed in a tube furnace under a reducing atmosphere of FG. The system was initially purged with FG at a flow rate of 60 sccm for one hour, followed by a reduction to 20 sccm prior to temperature ramping. The samples were heated at a rate of 200 °C hr⁻¹ to the target annealing temperature, followed by isothermal annealing for durations of up to 100 hours.

Materials characterizations

XAS measurements were carried out at the 2 A beamline of the Pohang Accelerator Laboratory using TEY mode at 300 K⁵⁷. For accurate comparison, the Fe and Co *L*-edge spectra were normalized to the intensity of their respective *L*₃-edges, while the O *K*-edge spectra were normalized to the background and the absorption edge near 565 eV. Multiplet fitting of the Fe and Co *L*-edge XAS spectra was performed using CTM4XAS, a ligand-field multiplet simulation code for TMOs, to estimate oxidation states from linear combinations of reference spectra. Optical conductivity spectra were acquired by spectroscopic ellipsometry in the photon energy range of 0.75–6.0 eV near the Brewster angle at room temperature⁵⁸. To examine the feasibility of redox-driven structural reversibility in SrFe_{0.5}Co_{0.5}O_x films, in situ X-ray diffraction and resistance measurements were performed

simultaneously using a dome stage (Nextron XRDMPS-CH). To evaluate the redox reversibility, in situ cycling experiments were conducted by alternately switching the gas environment between FG and O₂ at 400 °C. Each gas cycle was maintained for several hours, and both structural and electrical responses were continuously monitored. These redox cycling experiments were repeated for up to six full cycles, confirming the phase reversibility and stability of the reduced and oxidized states (Fig. 5 and Supplementary Fig. 15). The dome chamber was interfaced with a high-resolution diffractometer and equipped with mass flow controllers to precisely regulate gas atmosphere and a PID controller for temperature stability. HAADF-STEM images and EDS element maps were obtained using a Cs-corrected STEM (Thermo Fisher Themis Z) operated at 300 kV. The convergence semi-angle and inner collection angle were set to 30 mrad and 50 mrad, respectively. Interatomic distances were quantified using custom python scripts. EEL spectral imaging was performed using a monochromated STEM (Thermo Fisher G2 Cube) operated at 80 kV. The convergence semi-angle was 13.5 mrad, and the full width at half maximum of the zero-loss peak was ~250 meV during spectral imaging.

Theoretical analysis

All DFT calculations of SrBO_x ($B = \text{Co, Fe}$) were carried out using the plane-wave-based Vienna Ab initio Simulation Package VASP^{59,60} version 5.4.4, within the generalized gradient approximation (GGA) using the Perdew–Burke–Ernzerhof for solids (PBEsol) exchange–correlation functional⁶¹. The energy cutoff for the plane-wave basis set was 600 eV, employing projected augmented wave potentials^{62,63}. A $6 \times 6 \times 2$ *k*-point mesh was utilized for sampling the Brillouin zone for a 36-atom unit cell and scaled linearly with the supercell size. We used a $2 \times 2 \times 1$ supercell for all calculations to accommodate Fe-Co solid solution on *B*-site and decrease periodic effects. The bulk geometry was optimised with a force convergence criterion of 1 meV/Å, and the individual components of the stress tensor were converged to ≤ 0.1 kBar. Magnetism of *B*-site cations, Co, and Fe was treated with the PBEsol collinear spin density approximation in the GGA with an onsite Hubbard *U* (GGA + *U*) scheme⁶⁴. An onsite Coulomb parameter $U = 4$ eV was applied for all *B*-site cations (Co and Fe) to account for the increased Coulomb repulsion between the semi-filled 3d states⁶⁵. The magnetic moments of *B*-site cations were initiated in the G-type antiferromagnetic state spins antiferromagnetically aligned within (001) planes between adjacent (001) planes⁶⁶.

Data availability

The data supporting the main figures generated in this study are available at Figshare: <https://doi.org/10.6084/m9.figshare.28944977>.

References

- Myung, J. H., Neagu, D., Miller, D. N. & Irvine, J. T. Switching on electrocatalytic activity in solid oxide cells. *Nature* **537**, 528–531 (2016).
- Wan, L. F., Inconvati, J. T., Poeppelmeier, K. R. & Prendergast, D. Building a fast lane for Mg diffusion in α -MoO₃ by fluorine doping. *Chem. Mater.* **28**, 6900–6908 (2016).
- Acharya, S. K. et al. Epitaxial brownmillerite oxide thin films for reliable switching memory. *ACS Appl Mater. Interfaces* **8**, 7902–7911 (2016).
- Yang, Q. et al. Solid-state electrochemical thermal transistors. *Adv. Funct. Mater.* **33**, 2214939 (2023).
- Li, D. et al. Superconductivity in an infinite-layer nickelate. *Nature* **572**, 624–627 (2019).
- Goodenough, J. B. Electronic and ionic transport properties and other physical aspects of perovskites. *Rep. Prog. Phys.* **67**, 1915–1993 (2004).
- Bertaut, E. F., Blum, P. & Sagnieres, A. Structure du ferrite bicalcique et de la brownmillerite. *Acta Cryst.* **12**, 149–159 (1959).
- Jeen, H. et al. Reversible redox reactions in an epitaxially stabilized SrCoO_x oxygen sponge. *Nat. Mater.* **12**, 1057–1063 (2013).
- Tsujimoto, Y. et al. Infinite-layer iron oxide with a square-planar coordination. *Nature* **450**, 1062–1065 (2007).
- Khare, A. et al. Topotactic metal-insulator transition in epitaxial SrFeO_x thin films. *Adv. Mater.* **29**, 1606566 (2017).
- Tikhonovich, V., Naumovich, E., Logvinovich, D., Kharton, V. & Vecher, A. Oxygen deficiency and phase transitions in SrCo_{1-x-y}Fe_xCr_yO_{3-δ} (x = 0.10–0.40, y = 0–0.05). *J. Solid State Electrochem.* **7**, 77–82 (2003).
- Lee, J. et al. Redox-driven nanoscale topotactic transformations in epitaxial SrFe_{0.8}Co_{0.2}O_{3-x} under atmospheric pressure. *Phys. Rev. Appl.* **10**, 054035 (2018).
- Kim, W. J. et al. Geometric frustration of Jahn–Teller order in the infinite-layer lattice. *Nature* **615**, 237–243 (2023).
- Li, H.-B. et al. Dehydration of electrochemically protonated oxide: SrCoO₂ with square spin tubes. *J. Am. Chem. Soc.* **143**, 17517–17525 (2021).
- Hayward, M. A. & Rosseinsky, M. J. Materials chemistry: cool conditions for mobile ions. *Nature* **450**, 960 (2007).
- Bian, Z. et al. Solid-state electrochemical thermal transistors with strontium cobaltite–strontium ferrite solid solutions as the active layers. *ACS Appl. Mater. Interfaces* **15**, 23512–23517 (2023).
- Khare, A. et al. Directing oxygen vacancy channels in SrFeO_{2.5} epitaxial thin films. *ACS Appl Mater. Interfaces* **10**, 4831 (2018).
- Li, Q. et al. Structural stability of Lanthanum-based oxygen-deficient perovskites in redox catalysis: a density functional theory study. *Catal. Today* **347**, 142–149 (2020).
- He, S. et al. La_{0.6}Sr_{0.4}CoO_{3-δ} films under deoxygenation: Magnetic and electronic transitions are apart from the structural phase transition. *Adv. Funct. Mater.* **34**, 2313208 (2024).
- Jeen, H. et al. Topotactic phase transformation of the brownmillerite SrCoO_{2.5} to the perovskite SrCoO_{3-δ}. *Adv. Mater.* **25**, 3651 (2013).
- Ichikawa, N. et al. Reduction and oxidation of SrCoO_{2.5} thin films at low temperatures. *Dalton Trans.* **41**, 10507–10510 (2012).
- Jin, L. et al. Understanding structural incorporation of oxygen vacancies in perovskite cobaltite films and potential consequences for electrocatalysis. *Chem. Mater.* **34**, 10373–10381 (2022).
- Abbate, M. et al. Controlled-valence properties of La_{1-x}Sr_xFeO₃ and La_{1-x}Sr_xMnO₃ studied by soft-x-ray absorption spectroscopy. *Phys. Rev. B* **46**, 4511–4519 (1992).
- Hu, Z. et al. Difference in spin state and covalence between La_{1-x}Sr_xCoO₃ and La_{2-x}Sr_xLi_{0.5}Co_{0.5}O₄. *J. Alloy Compd.* **343**, 5–13 (2002).
- Stavitski, E. & De Groot, F. M. The CTM4XAS program for EELS and XAS spectral shape analysis of transition metal L edges. *Micron* **41**, 687–694 (2010).
- Hirai, K. et al. Strain-induced significant increase in metal-insulator transition temperature in oxygen-deficient Fe oxide epitaxial thin films. *Sci. Rep.* **5**, 6 (2015).
- Tassel, C. & Kageyama, H. Square planar coordinate iron oxides. *Chem. Soc. Rev.* **41**, 2025–2035 (2012).
- Chowdhury, S. et al. High-temperature insulating ferromagnetic state in charge-disproportionated and spin-state-disproportionated strained SrCoO_{2.5} thin film. *APL Mater.* **12**, 051129 (2024).
- Vieten, J. et al. Redox behavior of solid solutions in the SrFe_{1-x}Cu_xO_{3-δ} system for application in thermochemical oxygen storage and air separation. *Energy Technol.* **7**, 131–139 (2019).
- Fujishiro, F., Oshima, N., Sakuragi, T. & Oishi, M. Oxygen desorption properties of perovskite-type SrFe_{1-x}Co_xO_{3-δ}: B-site mixing effect on the reduction properties of Fe and Co ions. *J. Solid State Chem.* **312**, 123254 (2022).
- Karvonen, L. et al. and Co-L XANES study on oxygen intercalation in perovskite SrCoO_{3-δ}. *Chem. Mater.* **22**, 70–76 (2010).
- Che, Q. et al. Operando soft X-ray absorption of LaMn_{1-x}Co_xO₃ perovskites for CO oxidation. *ACS Catal.* **14**, 11243–11251 (2024).
- Suntivich, J. et al. Design principles for oxygen-reduction activity on perovskite oxide catalysts for fuel cells and metal–air batteries. *Nat. Chem.* **3**, 546–550 (2011).
- Sayle, T. X. T., Parker, S. C. & Catlow, C. R. A. The role of oxygen vacancies on ceria surfaces in the oxidation of carbon monoxide. *Surf. Sci.* **316**, 329 (1994).
- Lu, G., Linsebigler, A. & Yates, J. T. Jr Photooxidation of CH₃Cl on TiO₂ (110): a mechanism not involving H₂O. *J. Phys. Chem.* **99**, 7626–7631 (1995).
- Henderson, M. A., Epling, W. S., Perkins, C. L., Peden, C. H. F. & Diebold, U. Interaction of molecular oxygen with the vacuum-annealed TiO₂(110) surface: molecular and dissociative channels. *J. Phys. Chem. B* **103**, 5328 (1999).
- Campbell, C. T. & Peden, C. H. Oxygen vacancies and catalysis on ceria surfaces. *Science* **309**, 713–714 (2005).
- Yang, C. W. et al. Chemical activity of oxygen vacancies on ceria: a combined experimental and theoretical study on CeO₂(111). *Phys. Chem. Chem. Phys.* **16**, 24165–24168 (2014).
- Schaub, R. et al. Oxygen vacancies as active sites for water dissociation on rutile TiO₂(110). *Phys. Rev. Lett.* **87**, 266104 (2001).
- Takeda, Y. et al. Phase relation and oxygen-non-stoichiometry of perovskite-like compound SrCoO_x (2.29 < x < 2.80). *Z. Anorg. Allg. Chem.* **540**, 259 (1986).
- Long, Y. W., Kaneko, Y., Ishiwata, S., Taguchi, Y. & Tokura, Y. Synthesis of cubic SrCoO₃ single crystal and its anisotropic magnetic and transport properties. *J. Phys. Condens. Matter* **23**, 245601 (2011).
- Radaelli, P. G. & Cheong, S.-W. Structural phenomena associated with the spin-state transition in LaCoO₃. *Phys. Rev. B* **66**, 094408 (2002).
- Choi, W. S. et al. Reversal of the lattice structure in SrCoO_x epitaxial thin films studied by real-time optical spectroscopy and first-principles calculations. *Phys. Rev. Lett.* **111**, 097401 (2013).
- Yang, Q. et al. Unusually large thermopower change from +330 to –185 μV K⁻¹ of brownmillerite SrCoO_{2.5}. *ACS Appl Electron Mater.* **2**, 2250–2256 (2020).
- Lee, J. H. et al. Strongly coupled magnetic and electronic transitions in multivalent strontium cobaltites. *Sci. Rep.* **7**, 8 (2017).
- Posadas, A. B., Lin, C., Demkov, A. A. & Zollner, S. Bandgap engineering in perovskite oxides: Al-doped SrTiO₃. *Appl Phys. Lett.* **103**, 142906 (2013).
- Takeda, Y. et al. Phase relation in the oxygen nonstoichiometric system, SrFeO_x (2.5 ≤ x ≤ 3.0). *J. Solid State Chem.* **63**, 237 (1986).

48. Jia, T. et al. The influence of oxygen vacancy on the electronic and optical properties of $\text{ABO}_{3-\delta}$ (A = La, Sr, B = Fe, Co) perovskites. *Phys. Chem. Chem. Phys.* **21**, 20454–20462 (2019).
49. Fazl-Ur-Rahman, K. & Periyasamy, G. Role of oxygen vacancy ordering on structure and reactivity of iron-doped Sr-based perovskites: a computational study. *J. Solid State Chem.* **317**, 123734 (2023).
50. Darwish, M. & Pohl, L. Insulator metal transition-based selector in crossbar memory arrays. *Electron Mater.* **5**, 17–29 (2024).
51. Hu, G. et al. Cu/MgO-based resistive random access memory for neuromorphic applications. *Appl. Phys. Lett.* **124**, 142109 (2024).
52. Steele, B. C. & Heinzl, A. Materials for fuel-cell technologies. *Nature* **414**, 345–352 (2001).
53. Ohta, H. et al. Giant thermoelectric Seebeck coefficient of a two-dimensional electron gas in SrTiO_3 . *Nat. Mater.* **6**, 129–134 (2007).
54. Choi, H. et al. Organometal halide perovskite-based photoelectrochemical module systems for scalable unassisted solar water splitting. *Adv. Sci.* **10**, 2303106 (2023).
55. Lu, N. P. et al. Electric-field control of tri-state phase transformation with a selective dual-ion switch. *Nature* **546**, 124–128 (2017).
56. Kareev, M. et al. Atomic control and characterization of surface defect states of TiO_2 terminated SrTiO_3 single crystals. *Appl. Phys. Lett.* **93**, 061909 (2008).
57. Abbate, M. et al. Probing depth of soft x-ray absorption spectroscopy measured in total-electron-yield mode. *Surf. Interface Anal.* **18**, 65–69 (1992).
58. Aspnes, D. E. Spectroscopic ellipsometry - past, present, and future. *Thin Solid Films* **571**, 334–344 (2014).
59. Kresse, G. & Furthmüller, J. Efficiency of ab-initio total energy calculations for metals and semiconductors using a plane-wave basis set. *Comput. Mater. Sci.* **6**, 15–50 (1996).
60. Kresse, G. & Furthmüller, J. Efficient iterative schemes for ab initio total-energy calculations using a plane-wave basis set. *Phys. Rev. B* **54**, 11169–11186 (1996).
61. Perdew, J. P. et al. Restoring the density-gradient expansion for exchange in solids and surfaces. *Phys. Rev. Lett.* **100**, 039902 (2008).
62. Blochl, P. E. Projector augmented-wave method. *Phys. Rev. B* **50**, 17953 (1994).
63. Kresse, G. & Joubert, D. From ultrasoft pseudopotentials to the projector augmented-wave method. *Phys. Rev. B* **59**, 1758–1775 (1999).
64. Dudarev, S. L., Botton, G. A., Savrasov, S. Y., Humphreys, C. J. & Sutton, A. P. Electron-energy-loss spectra and the structural stability of nickel oxide: an LSDA+U study. *Phys. Rev. B* **57**, 1505–1509 (1998).
65. Nakayama, K. et al. Transition-metal distribution in brownmillerite $\text{Ca}_2\text{FeCoO}_5$. *Inorg. Chem.* **58**, 10209–10216 (2019).
66. Battle, P. D., Gibb, T. C. & Lightfoot, P. The crystal and magnetic structures of $\text{Sr}_2\text{CoFeO}_5$. *J. Solid State Chem.* **76**, 334–339 (1988).

Acknowledgements

This work was supported by the National Research Foundation of Korea (NRF) grant funded by the Korean government (MSIT) (RS-2025-00558200). Also, this work was partially supported under the framework of the international cooperation program managed by the NRF (NRF-2022K2A9A1A01098180). First-principles calculations (V.R.C. and K.P.) were supported by the U.S. Department of Energy, Office of Science, Basic Energy Sciences, Materials Science and Engineering Division. We acknowledge computational resources provided by the National Energy Research Scientific Computing Centre (NERSC), which is supported by the Office of Science of the U.S. Department of Energy under Contract No. DE-AC02-05CH11231 using NERSC award BES-

ERCAP-m1057. H.O. is supported by Grants-in-Aid for Scientific Research A (22H00253) from the Japan Society for the Promotion of Science (JSPS). Part of this work was supported by the Crossover Alliance to Create the Future with People, Intelligence and Materials, and by the Network Joint Research Centre for Materials and Devices. H.J. acknowledges the support of the Korea Basic Science Institute (National Research Facilities and Equipment Centre) grant funded by the Ministry of Education (grant No. RS-2024-00435344). S.P. and S.Y. acknowledge support from the Nano & Material Technology Development Program through the National Research Foundation of Korea (NRF), funded by the Ministry of Science and ICT (RS-2024-00460372). We thank Nextron Corporation for the generous technical support.

Author contributions

J.L. synthesized the samples and conducted in situ XRD experiments with H.C., S.R., and J.C. Optical measurements and analysis were performed by J.L. and Y.S. XAS experiments and their interpretation were carried out by J.L. and Y.K. K.C.P. and V.R.C. performed first-principles calculations. In-plane XRD patterns were measured by G.K. and H.O. S.P. and S.Y. conducted STEM, EELS, and EDS experiments and analyses. H.J. initiated and supervised the project. All authors contributed to the discussion of results and writing of the manuscript.

Competing interests

The authors declare no competing interests.

Additional information

Supplementary information The online version contains supplementary material available at <https://doi.org/10.1038/s41467-025-62612-1>.

Correspondence and requests for materials should be addressed to Hyoungeon Jeon.

Peer review information *Nature Communications* thanks Chonglin Chen, Woo Seok Choi, Felix Gunkel, and the other, anonymous, reviewer(s) for their contribution to the peer review of this work. A peer review file is available.

Reprints and permissions information is available at <http://www.nature.com/reprints>

Publisher's note Springer Nature remains neutral with regard to jurisdictional claims in published maps and institutional affiliations.

Open Access This article is licensed under a Creative Commons Attribution-NonCommercial-NoDerivatives 4.0 International License, which permits any non-commercial use, sharing, distribution and reproduction in any medium or format, as long as you give appropriate credit to the original author(s) and the source, provide a link to the Creative Commons licence, and indicate if you modified the licensed material. You do not have permission under this licence to share adapted material derived from this article or parts of it. The images or other third party material in this article are included in the article's Creative Commons licence, unless indicated otherwise in a credit line to the material. If material is not included in the article's Creative Commons licence and your intended use is not permitted by statutory regulation or exceeds the permitted use, you will need to obtain permission directly from the copyright holder. To view a copy of this licence, visit <http://creativecommons.org/licenses/by-nc-nd/4.0/>.

© The Author(s) 2025